Longwavelength InAsSb Infrared Photodetectors

ARPA project #   N00014-93-1-0931
ONR No. N00014-92-J-1951
ONR No. N00014-93-1-0409

Principal Investigator: Manijeh Razeghi

Center for Quantum Devices
Northwestern University, Evanston, IL 60208

Background and theory
  Staff: Dr. J. Piotrowski

MOCVD growth
  Staff: Dr. J. Xu
  Students: J. Kim, D. Wu, J. Wojkowski

Detector processing
  Staff: Dr. J. Xu

Detector measurements
  Staff: Dr. J. Xu, Dr. J. Piotrowski
  Students: J. Kim

April 1995

Longwavelength (8-14 μm) InAsSb heterostructure photodetectors

Outline

Objectives

This work was intended to explain basic questions related to long-wavelength InAsSb photodetectors

- Can InAsSb be used for IR photodetectors operating at 200-300 K in the entire 8-14 μm region?
- What is the photoconductivity lifetime?
- What are limitations to the performance of InAsSb photoconductive and photovoltaic detectors? What are the limits?
- Can InAsSb compete with HgCdTe in applications for LWIR photodetectors?
- Demonstration of near room temperature 10.6 μm IR photodetector
- What should be done to improve the performance further?
- How to obtain focal plane array

1. Introduction

$InAs_{1-x}Sb_x$ has been of great interest for long-wavelength infrared detector applications as an alternative to $Hg_{1-x}Cd_xTe$, which suffers from instability problems. The inherent stability, very good semiconductor properties, and possible use of industry standard technologies (MBE and MOCVD) makes this material a primary candidate for application in infrared detectors. The main problem to be solved is the extension of operation to long-wavelength. Although having the smallest bandgap among III-V semiconductors, InAsSb was believed not to cover the entire 8-12 μm spectral range at 77 K because the optical absorption edge can go up only to $\lambda_g \approx 10$ μm. So there has been a lot of efforts to

1

shift the absorption edge to longer wavelength using strained layer superlattice. However, the quantum well and superlattice photodetectors offer no fundamental advantages in terms of ultimate performance if a suitable "bulk" narrow gap semiconductor can be found. Moreover, superlattice devices suffer from their own problems including stability, reproducibility, uniformity and cost of production.

InAsSb seems to be particularly interesting for near room temperature applications. While early studies have established a maximum cutoff wavelength of ≈ 12 μm at 300 K, the recent results indicate the possibility of a cutoff wavelength of the epitaxial films to be larger than 12.5 μm. Our recent studies has shown an efficient band-to-band absorption of 500 cm^{-1} at room temperature for wavelengths as long as 15 μm with p-type InAs$_{0.35}$Sb$_{0.65}$. This may be due to the ordering effects but the exact mechanism has not been understood yet.

Performance of long-wavelength IR photodetectors operating at near room temperature is limited mainly by the high thermal generation and recombination rates. High thermal generation and recombination rates result in a high noise. Furthermore, high recombination rate reduces the photoresponse.

Some solutions have been proposed to reduce the thermal generation noise without cooling. First, optimizing the doping and energy gap profiles has been suggested as a way to improve the performance of semiconductor photodetectors at room-temperature maximizing the optical generation rate compared to thermal generation rate. Secondly, the thermal generation rate can be reduced by using the non-equilibrium mode of operation in which carrier concentrations are brought below their equilibrium. Another possibility is to reduce the actual volume of a photodetector but without sacrificing quantum efficiency and keeping the apparent optical area of the devices unchanged.

2. Theoretical performance of infrared photodetectors

2.1. Theoretical model

Let us consider a generalized model applicable to any type of a photodetector. The device is a slab of homogeneous semiconductor with the actual "electrical" area A_e coupled to the beam of infrared radiation by its optical area A_o. (Fig. 1). Usually, the optical and electrical areas of the device are the same or close. However, the use of an optical concentrator can increase the A_o/A_e ratio.
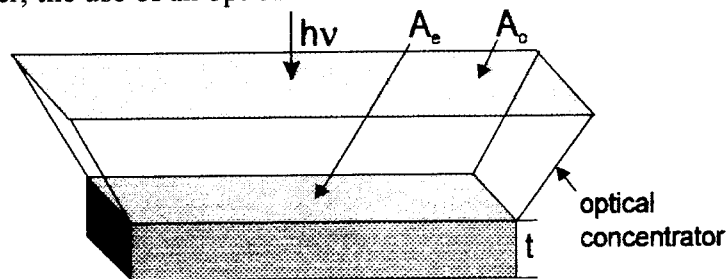
Fig. 1. Model of a photodetector.

The current responsivity of the photodetector is determined by both the quantum efficiency η and the photoelectric gain g. The quantum efficiency value describes how well the detector is coupled to the radiation to be detected. It is usually defined as the number of electron-hole pairs generated per incident photon. The photoelectric gain is the number of carriers passing contacts per one generated pair. This value shows how well the generated electron-hole pairs are used to generate current response of a photodetector. Both values are assumed here as constant over the volume of the device.
The spectral current responsivity is

2

$$R_i = \frac{\lambda \eta}{hc} qg \qquad (1)$$

where λ is the wavelength, h is the Planck constant, c is the light velocity, q is the electron charge and g is the photoelectric current gain. Assuming that the current gains for photocurrent and noise current are the same, the current noise due to the statistical nature of generation and recombination processes is

$$I_n^2 = 2(G+R)A_e t\Delta f q^2 g^2 \qquad (2)$$

where G and R are the generation and recombination rates, Δf is the frequency band and t is the thickness of the slab.

The effects of a fluctuating recombination can frequently be avoided by arranging for the recombination process to take place in a region of the device where it has little effect due to low photoelectric gain: for example, at the contacts in sweep-out photoconductors or in the neutral regions of diodes. In this case, the noise can be reduced by a factor of $2^{1/2}$. The generation process with its associated fluctuation, however, cannot be avoided by any means. Detectivity D* is the main parameter characterizing normalized signal to noise performance of detectors. According to Eqns. (1-2)

$$D^* = \frac{\lambda}{hc}\left(\frac{A_o}{A_e}\right)^{1/2}\left(\frac{\eta}{t^{1/2}}\right)\{2(G+R)\}^{-1/2}. \qquad (3)$$

For a given wavelength and operating temperature, the highest performance can be obtained by maximizing $\eta^2/t(G+R)$ which corresponds to the condition of the highest ratio of the optical generation rate to the square root of the thermal generation-recombination rate.

For effective absorption of infrared radiation, a semiconductor material having a narrower band gap compared to the photon energy must be used. This means that narrow gap semiconductors are required for long and middle-wavelength devices. The direct consequence is that at room temperature the thermal energy of charge carriers kT becomes comparable to the band gap. This causes band-to-band transitions making the thermal generation and recombination rates very high. As a result, conventional long-wavelength detectors are very noisy when operating at near room temperature. To achieve a high performance, the thermal generation and recombination must be suppressed to the lowest possible level. This is usually done with cryogenic cooling of the photodetector.

2.2. Equilibrium mode

At high temperatures, generation-recombination processes in narrow gap semiconductors are dominated by the Auger mechanism. Let us consider the Auger limited detectivity of photodetectors. At equilibrium, the generation and recombination rates are equal. Assuming that both rates contribute to noise,

$$D^* = \frac{\lambda}{2hc}\left(\frac{A_o}{A_e}\right)^{1/2}\frac{\eta}{t^{1/2}}G_A^{-1/2} \qquad (4)$$

3

where G_A is the Auger generation rate. Further discussions are applicable to semiconductors having a similar band structure as InSb (e.g. InAsSb, InTlSb, HgCdTe and many other narrow gap semiconductors). For non-degenerate statistics

$$G_A = \frac{n}{2\tau_{A1}^i} + \frac{p}{2\tau_{A7}^i} = \frac{1}{2\tau_{A1}^i}(n + \frac{p}{\gamma}) \qquad (5)$$

where n and p are the electron and hole concentrations, τ_{A1}^i and τ_{A7}^i are the intrinsic Auger 1 and Auger 7 recombination times and γ is the ratio of Auger 7-to-Auger 1 intrinsic recombination times. The Auger-dominated detectivity is

$$D^* = \frac{\lambda}{2^{1/2}hc}\left(\frac{A_o}{A_e}\right)^{1/2}\frac{\eta}{t^{1/2}}\left(\frac{\tau_{A1}^i}{n + p/\gamma}\right)^{1/2} \qquad (6)$$

The resulting Auger generation achieves its minimum for $p = \gamma^{1/2}n_i$. Since $\gamma > 1$, the highest detectivity of Auger limited photodetectors can be achieved with a p-type doping. In practice, the low p-type doping level required for cooled devices would be difficult to achieve. At low temperatures, the p-type devices also suffer from some non-fundamental limitations (contacts, surface, Shockley-Read processes) more than the n-type ones. This is the reason why low-temperature photoconductors are typically manufactured from lightly doped n-type materials. In contrast, p-type doping is clearly advantageous for the near room temperature and long-wavelength photodetectors.

At near room temperature, the electron and hole concentrations in narrow gap semiconductors are equal to the intrinsic concentration. The decrease of temperature strongly increases τ_{A1}^i and decreases the intrinsic concentration, sharply improving D*. At lower temperatures when the concentration of majority carriers saturates at an extrinsic level, the performance still improves with decreasing temperature due to increasing τ_{A1}^i. For a given wavelength and temperature of operation, the performance can be maximized by selection of gap doping and thickness of the detector as follows from Eqn. (6).

As calculations show, the liquid nitrogen cooling makes it possible to achieve BLIP performance in the whole 2–20 μm range; while 200 K cooling, which is achievable with Peltier coolers, would be sufficient for BLIP operation in the middle and short wavelength regions (< 5 μm).

2.3. Reduced volume devices

Another way to improve the performance is to reduce the detector volume by reduction of thickness and its actual area. This must be done without decreasing the quantum efficiency and preserving the required optical area of a detector.

The $\eta/t^{1/2}$ term. Since the detectivity is proportional to the factor $\eta/t^{1/2}$, a high quantum efficiency must be achieved in thin devices. This is usually difficult to realize in practice for devices operating at near room temperatures as the absorption of long-wavelength radiation in narrow gap semiconductors is weak for gaps close to the photon energy. The quantum efficiency can be enhanced in thin devices with non-reflective frontside and highly reflective backside surfaces of the sensitive element. This can be achieved in a multilayer structure, in which the semiconductor flake is sandwiched between two dielectric layers and a backside metal reflecting mirror. The effective absorption can be improved further using the interference effect to set up the resonant cavity within the photodetector. It should be noted that the interference effects can be applied only in narrow spectral regions.

4

The A_o/A_e term. A possible way to achieve an effective concentration of radiation is to immerse the photodetector to the hemispherical or hyperhemispherical lenses as shown in Fig. 2. Due to immersion, the linear size of the detector increases by a factor of n and n^2 for hemispherical and hyperhemispherical lens, respectively. As a result, the detectivity is increased by the same factor. The practical use of immersion technology has been limited due to problems in mechanical matching of detector and lens material and severe transmission and reflection losses. Another limitation is due to the limited acceptance angle of the devices as a result of the total reflection at the lens-glue interface. The problems have been recently solved by using monolithic technology based on epitaxy of $Hg_{1-x}Cd_xTe$ on $(Cd,Zn)Te$ substrate. A similar approach can be used for epilayers deposited on GaAs substrates.

The gain factors achieved with hyperhemispherical immersion are substantially higher compared to those for hemispherical immersion. The hyperhemispherical immersion may restrict the acceptance angle of the detector and require more severe manufacturing tolerances. These restrictions depend on the refraction coefficient of the lens. For $(Cd,Zn)Te$ (n=2.7) and GaAs (n=3.4) substrates, the restrictions are not as severe as for germanium lenses, however, and have no practical importance in most cases.
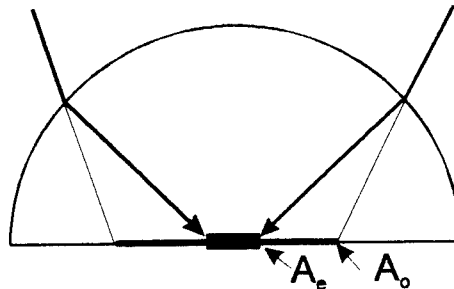

Fig. 2. Principle of optical immersion.

Some gains due to optical immersion are specific for particular types of photodetectors. For example, the reduction of bias power dissipation is important in cases of photoconductors or some types of photodiodes which require strong bias for the best performance. The immersion also significantly reduces the heat load of heat sinks and cooling devices making it possible to reduce size, weight, price, and power consumption of cooling systems.

2.4. 3-D heterostructure photodetector

An optimized photodetector should ensure the best ratio of the optical generation to square thermal generation. Therefore, any parasitic thermal generations and recombinations should be suppressed. Such a device should consist of the following regions as shown in Fig. 3:

- Lightly doped narrow gap semiconductor region which is the main part of the detector. It acts as an absorber of IR radiation where electron-hole pairs are generated. Its band gap, doping, and geometry should be selected for the highest ratio of the optical generation rate to the sheet thermal generation rate.
- Electric contacts to the narrow gap region which sense optically generated charge carriers. Contacts should not contribute to the dark current of the device.
- Passivation of the narrow gap region. The surfaces of the absorber regions must be insulated from the ambient by a material which also does not contribute to the generation of carriers. In addition, the carriers which are optically generated in the absorber are kept away from surfaces, where

5

recombination can reduce the quantum efficiency. For the best sensitivity, the frontside face should perfectly transmit while the backside face should perfectly reflect IR radiation.

- Concentrator of IR radiation and backside mirror for the highest quantum efficiency.
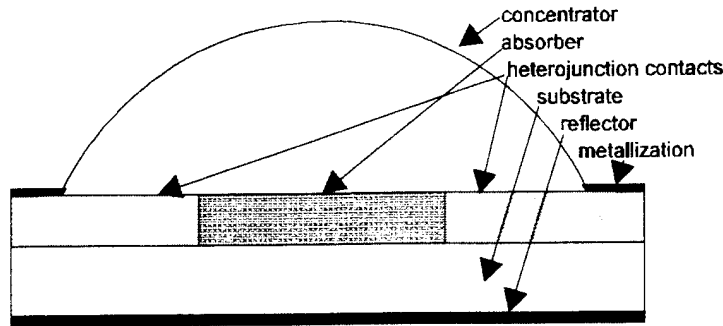

Fig. 3. Schematic of a 3D heterostructure photodetector.

In practice, such a device can be obtained using 3-dimensional gap and doping engineering with the narrow gap absorber buried in a wide gap semiconductor. The undoped wide gap material can be used as a front face, as a window and/or concentrator of incoming radiation. Doped wider gap semiconductors can be used for contacts. In some applications, degenerate narrow gap n-type (n$^+$) regions can be used for contacts and windows since their effective energy gap is increased due to the Burstein-Moss effect. The device must be also supplied with contact metallization to wide gap contact regions.

2.5. Photoconductors
According to the simple theory of photoconductivity, the voltage responsivity is

$$R_v = \frac{q\lambda}{hc}\frac{\eta\mu_e\tau V_b}{l^2}\left(1+\frac{1}{b}\right)$$ (7)

where q is the electron charge, h is the Planck constant, c is the light velocity, λ is the wavelength, g is the photoconductive gain, η is the quantum efficiency, b is the electron-to-hole mobility ratio, l is the detector length, and V_b is the bias voltage.

The Johnson noise limited detectivity is

$$D^* = \frac{R_v(A\Delta f)^{1/2}}{(4kTR)^{1/2}}$$ (8)

The generation-recombination limit of detectivity can be achieved if generation-recombination noise is much higher compared to the Johnson noise. In this case,

$$D^* = \frac{\lambda\eta}{2hc(tG)^{1/2}}$$ (9)

where G is the thermal generation rate. We can see that a high value of lifetime is necessary for the highest detectivity. Strong biasing may be required for generation-recombination noise to dominate over

6

the Johnson noise. The problem is stringent in devices with low recombination time such as long-wavelength photodetectors operating at near room temperatures.

Another limitation results from the low frequency noise. In strong biased photoconductors, the low frequency noise may dominate up to high frequencies.

Apart from bulk generation-recombination processes, lifetime is often limited by non-fundamental thermal generation-recombination processes at surfaces and contact regions.

2.6. Photovoltaic detectors

Photoconductivity is the most simple mode of operation of IR photodetectors. Photovoltaic detectors offer important advantages, however.

1. PV detectors offer the same or better fundamental limit of performance. For example, the noise due to recombination can be prevented by arranging the recombination to take place in regions which do not contribute to the noise (neutral regions of reverse biased photodiodes). As a result, the ultimate performance of PV detectors exceed that of photoconductors by a factor of $2^{1/2}$.

2. Long-wavelength photoconductors require a high bias current to achieve their optimum performance. This limits the possibility to use them for focal plane arrays. In contrast, photovoltaic detectors dissipate little or no heat. Therefore, they can be used for any element number FPA.

3. Response time of photoconductors is typically equal to recombination time. In contrast, photovoltaic detectors exhibit response times shorter than the recombination lifetimes.

4. Since they are non-biased, photovoltaic detectors do not exhibit low frequency noise and can operate with DC optical signal.

5. The improvement of performance by the non-equilibrium mode of operation is more efficient in extracted photodiodes than in excluded photoconductors.

Photovoltaic detectors have also some disadvantages.

1. Practical realization of high quality infrared photodiodes requires use of heterostructures with optimized band gap and doping profiles.

2. Near room temperature photodiodes exhibit extremely low junction resistances, often below series resistances and equivalent preamplifiers' noise resistances. This makes the potential performance difficult to achieve in practice.

It should be noted, however, the disadvantages are of technological rather than fundamental nature, and they can be overcome with the advent of newly developed technologies.

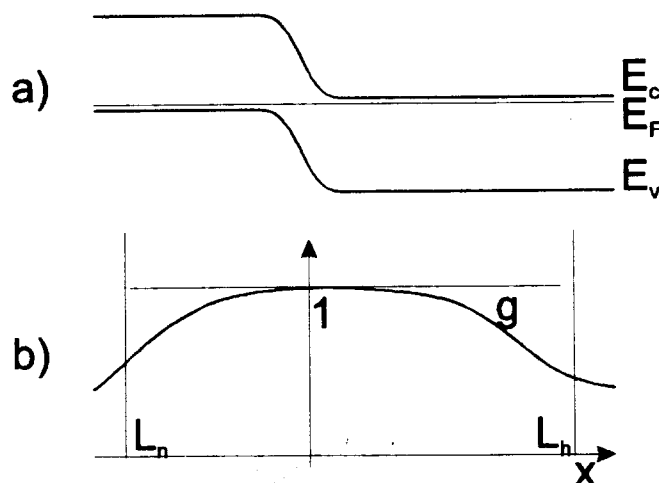Let us consider a p-n homojunction photovoltaic structure shown in the Fig. 4.

Fig. 4. Band diagram of p-n photodiode a) and distribution of photoelectric gain.

The photocurrent of a photodiode can be described as

$$I_{ph} = \int G_{op} qg dx \qquad (10)$$

For monochromatic radiation,

$$G_{op} = \frac{\lambda \alpha q}{hc} \Phi(x) \qquad (11)$$

Therefore,

$$I_{ph} = \int \frac{\lambda \alpha q}{hc} \Phi(x) g dx \qquad (12)$$

The current responsivity is the ratio of photocurrent to the radiant flux.

$$R_i = \frac{I_{ph}}{\Phi} = \frac{\int \frac{\lambda \alpha q}{hc} \Phi(x) g dx}{\Phi} \qquad (11)$$

The saturation dark current density is

$$I_d = \int G q g dx \qquad (12)$$

The current noise density is

$$I_n^2 = \int 2(G + G_{op} + R) q g dx \qquad (13)$$

For the highest possible detectivity, the ratio of the optical generation to the square root of thermal generation should be maximized. To achieve this:
- optical generation rate should be maximized
- thermal generation and recombination rates should be minimized
- the volume of non-zero photoelectric gain where thermal generation and recombination occurs should be minimized.

The optimization of the photovoltaic detector can be made by a selection of the compositional and doping profiles.

First, consider the case of p-n photodiode based on constant band gap material. The photoelectric gain is close to unity at distances equal to the corresponding diffusion length. To ensure a good photoresponse, the optical generation should occur at the locations with near unity photoelectric gain. The immediate requirement is for the illuminated side of the p-n junction to be thinner than the diffusion length.

Assuming that the absorption length is shorter compared to the diffusion length, the thickness of the device should be reduced to the absorption length to minimize the total thermal generation in the device. At near room temperatures, thermal generation and recombination in narrow gap semiconductors is determined by the Auger 1 and Auger 7 recombination processes.

8

In principle, the highest performance can be obtained using the n⁻p photodiodes, illuminated through the n⁺ region. Due to the Burstein-Moss effect, the cutoff wavelength is significantly shifted toward shorter wavelength, therefore n⁺ region is optically transparent and plays a role of optical window for IR radiation. At the same time, the Auger processes are largely suppressed, and the main contribution to the total dark current and noise comes from the limited volume of the p-type layer. The radiation is absorbed in the p-type region of the junction layer which plays a role of absorber material. The absorption occurs at the space charge region and in its vicinity at the depth of about $1/\alpha$ where the photoelectric gain is close to unity. In principle, the device makes it possible to obtain the highest performance for a given wavelength and operating temperature.
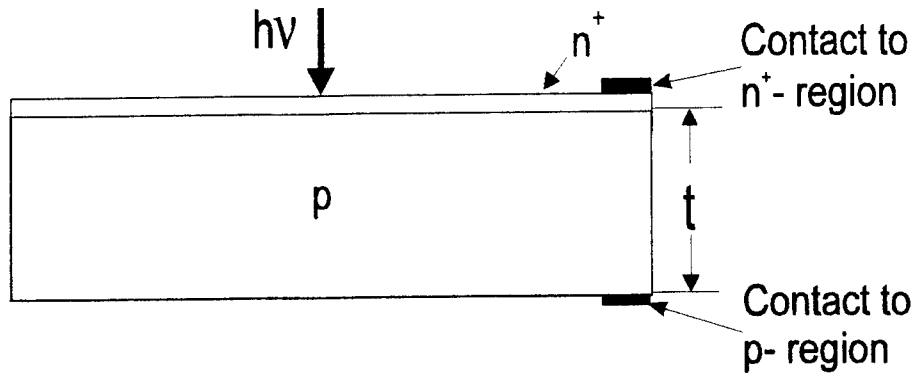

Fig. 5. The schematic of a n⁺p photodiode.

For the best performance, the doping of the p-type layer should produce a hole concentration of $p = \gamma^{1/2} n_i$. The thickness of the base region should be optimized for near unity quantum efficiency and a low dark current. This is achieved with a base thickness slightly higher than the inverse absorption coefficient $t = 1/\alpha$.

Consider a low-concentration p-type base layer with a degenerated n-type cap. The expressions describing such device are very simple. The current-voltage characteristic of the diffusion-limited photodiode can be described as

$$I = I_{ph} + I_s \left(e^{\frac{qV}{kT}} - 1 \right).$$

(14)

The current responsivity is

$$R_i = \frac{\lambda \eta q g}{hc}$$

(15)

where η is the quantum efficiency. Assuming that the saturation dark current is due only to thermal generation in the base layer and that its thickness is small compared to the diffusion length,

$$I_s = G t q A$$

(16)

where G is the generation rate in the base layer. The zero bias resistance-area product is

$$R_o A = \frac{AkT}{qI_s}$$

(17)

9

or

$$R_oA = \frac{kT}{q^2 Gt} \cdot \tag{18}$$

Photodiodes are typically operated at zero bias to minimize the heat load and for zero 1/f noise. At zero bias, the thermal generation and recombination rates are equal. The noise current due to thermal generation-recombination processes in the base layer is

$$I_s = GtqA \tag{19}$$

The normalized detectivity achieves its limit due to thermal generation in the p-region. The normalized detectivity is often expressed as a function of R_oA

$$D^* = \frac{\lambda \eta q}{hc} \cdot \frac{(R_oA)^{1/2}}{(4kT)^{1/2}} \tag{20}$$

For the best performance under the given operation conditions (wavelength, temperature), the value of $\eta(R_oA)^{1/2}$ should be maximized. The R_oA product is being used as the main factor which reflects the quality of the p-n junction.

Assuming the Auger mechanism in the extrinsic case,

$$R_oA = \frac{2kT\tau_{A7}^i}{q^2 N_A t} \tag{21}$$

$$D^* = \frac{\lambda}{2^{1/2} hc} \left(\frac{A_o}{A_e} \right)^{1/2} \frac{\eta}{t^{1/2}} \left(\frac{\tau_{A1}^i}{n + p/\gamma} \right)^{1/2} \tag{22}$$

As the last expression shows, the R_oA product can be decreased by reducing thickness of the base layer. Since $\gamma = \tau_{A7}^i / \tau_{A1}^i > 1$, higher R_oA value can be achieved in p-type base devices compared to that of n-type devices of the same doping level. Detailed analysis shows that the absolute maximum of R_oA is achievable with base layer doping producing $p = \gamma^{1/2} n_i$ which corresponds to the minimum of thermal generation.

The optimum doping depends on the intrinsic concentration. The required level is high for high-temperature and long-wavelength devices, and it can be easily obtained in practice. The low-temperature and short-wavelength devices require a very low doping of the base which may be difficult to achieve in practice.

Apart from the fundamental Auger generation in the $1/\alpha$ thick base region, the contributions may arise from non-fundamental sources due to the base and cap layers, depletion region and surface. In practice, the non-fundamental sources dominate the dark current of the present InSb and $Hg_{1-x}Cd_xTe$ photodiodes with the exception of specific cases of near room temperature devices and highest quality 80 K LWIR and 200 K MWIR devices. Densities greater than the mid 10^6 cm^{-3} of as-grown or process-induced dislocations severely degrade device performance by producing excess dark current.

The n^+p device with thin p-region is, however, extremely vulnerable to thermal generation and recombination processes at the backside surface. This can be prevented by suitable passivation. The device also suffers from high series resistances originating from high resistance of the p-region due to

both low hole mobility and low thickness. Another problem arises from the thermal generation and recombination at contact to p-region. The problems can be solved by the use of heterojunction contact to p-type region.

Fig. 6. shows the band diagram of the hypothetical heterojunction $\underline{n}^+\pi\underline{p}^-$ photovoltaic (the symbols denotes $\underline{n}^+$ heavy n-doped wide gap, π- lightly doped narrow gap and $\underline{p}^+$ heavy doped p-type regions). This device makes it possible to optimize the parameters of the narrow gap absorber region and the heavy doped contacts region independently and offers important advantages. Let us consider illumination from the n^+ side. Since the n^+ region is of wider gap, the radiation with quantum energy $E_g < h\nu < E_{gn}$ is absorbed only in the narrow gap semiconductor, predominantly in vicinity of the $\underline{n}^+\pi$ junction. This results in high quantum efficiency. The thermal generation can be limited to the absorber region only. Contacts to heavy doped regions do not contribute to the total thermal generation, since photoelectric gain is very low there due to short diffusion length in heavy doped regions.

A numerical technique has to be used to analyze properties of the heterostructures. The mathematical model employed consists of the two current density equations, two continuity equations and Poisson's equation which are collectively referred to as the Van Roosbroeck model. A self-consistent iterative procedure for the solution of this mathematical model has been reported in many papers. Here, we provide a semiquantitative piecemeal approach to assess the contribution of various regions to the total dark current.
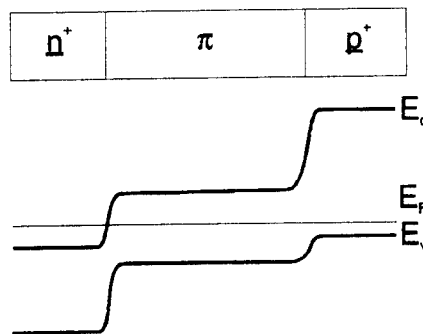

Fig. 6. Schematic band diagram of zero-biased $\underline{n}^+\pi\underline{p}^+$ photovoltaic detector.

The total dark current of the device consists of dark currents due to thermal generations in
1. absorber layer
2. n^+ layer
3. p^+ layer
4. interface regions

1. The dominant thermal generation mechanisms in the absorber region are the Auger 1, Auger 2 and possibly, Shockley-Read processes. The dark current is due to the bulk Auger thermal generation which sets the ultimate performance of the device operating in the equilibrium mode (zero bias).
2. The dominant thermal generation mechanism in the n^+ region is the Auger 1 process. The contribution of this region is usually very small due to both increased band gap and material degeneration.
3. The dominant thermal generation in the p^+ region is the Auger 7 and possibly, Shockley-Read processes. This region will dominate dark current unless band gap is increased compared to the absorber region. The valence band has a large density of states, therefore, an extremely high doping level would be necessary in p^+ region to achieve degeneracy and quenching of the Auger 7 mechanisms in narrow gap material. This is not possible to achieve in practice. The remaining solution is the use of wide gap material.

11

The contribution of this region to the total dark current can be reduced by proper selection of band gap, doping level, and type of dopants. Shallow dopants which do not introduce recombination centers should be used.

4. Some contribution to dark current may arise from generation in the transitions regions $\underline{n}^+\pi$ and $\pi\underline{p}^+$ regions if the junctions are graded and due to Debye tailing. The composition profiles in heterostructures are very sharp, and the gradient in the carrier concentrations is mostly due to the Debye tails. Calculation shows, that the contributions are relatively low.

3. Growth and characterization of Sb-based materials by MOCVD

Metalorganic chemical vapor deposition (MOCVD) is a non-equilibrium growth technique that has established itself as a unique and important epitaxial crystal technique. In comparison to other advanced growth techniques that include liquid phase epitaxy (LPE) and molecular beam epitaxy (MBE), MOCVD is the most economical and large-scale production adapted growth technique that is widely used in the industry. Moreover, it is most versatile: virtually all compound semiconductors and alloys have been grown including new and metastable materials such as InAsBi and InAsBiSb. Such attractive aspects of MOCVD make it an ideal growth technique for growing Sb-based III-V semiconductor layers.

In our research, low pressure (76 torr) MOCVD with horizontal reactor geometry has been used for material growth. All layers have been characterized by optical microscope (morphology), x-ray diffraction (structural), Hall measurement (electrical), ball polishing measurement (thickness), and Fourier transform infrared spectroscopy (FTIR, optical).

3.1 InSb

3.1.1 Growth

Trimethylindium (TMI) and trimethylantimony (TMSb) were used as precursors. Their respective bubbler temperatures were kept at 18 °C and 0 °C resulting in vapor pressures of 1.45 and 30.95 torr respectively. The growths were carried out on InSb, semi-insulating GaAs, and GaAs coated Si substrate. The latter was investigated because of the possibility for future integration of infrared detection and signal processing circuits on the same substrate. Superclean GaAs and GaAs/Si substrates were directly loaded into the growth chamber without any preparation. During the heating of the substrate, a pre-growth arsine overflow was maintained in order to prevent any surface degradation. For InSb substrates, the best preparation method was found to be etching in lactic acid and nitric acid (10:1) mixture. However, we observed that this etching reveals line defects on some InSb substrates. The line defects are believed to originate from the lapping-polishing stages of the substrate preparation.

The optimum InSb growth conditions were found by keeping the growth temperature constant and varying the V/III ratio. Based upon the surface morphology of InSb films, V/III ratio near 20 was found to be optimum at a growth temperature of 470 °C. Increase of V/III ratio resulted in poor crystallinity which was verified by large FWHM in x-ray diffraction spectra. Decrease in V/III ratio degraded the morphology, and indium droplets formed on the surface; the latter phenomenon was confirmed by dissolution of these droplets in hydrochloric acid, which preferentially etches indium.

3.1.2 Characterization

Under the optimum conditions, mirror-like InSb epilayers were grown on all substrates. With thickness of 3 μm, the film grown on InSb had x-ray FWHM of 16 arcsec while films grown on GaAs and GaAs/Si exhibited a FWHM of 208 and 304 arcsec, respectively. These FWHM values are among the best reported for InSb films of comparable thickness on the respective substrates, independently of the growth technology.
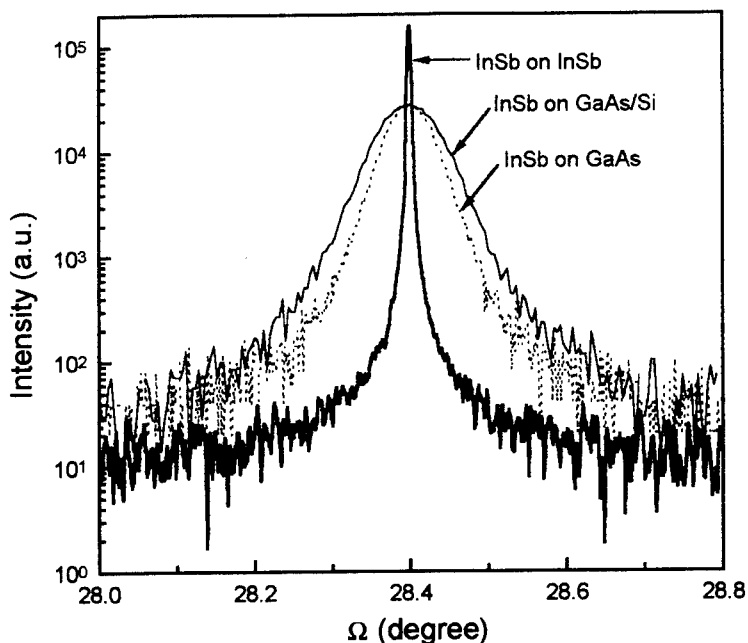

Fig. 7. X-ray diffraction spectra of 3 μm InSb peaks grown on different substrates.

A 3.6 μm-thick InSb films exhibited mobilities of 56,000 cm²/Vs at 300 K which increased to about 80,000 cm²/Vs at 77 K. Background carrier concentration was low 10^{15} cm^{-3} with n-type. Increase in Hall mobility and decrease in carrier concentration have been observed as the thickness of the layer is increased.

3.1.3 Doping

For the realization of photodetectors, control of both n and p-type doping is important. As an initial step, we achieved doping of InSb films. N and p-type doping of InSb was performed without any changes in the growth parameters.

N-type doping was achieved first by Si using silane (SiH_4) and disilane (Si_2H_4) and later by Sn using TESn. The TESn bubbler was kept at a temperature of -25 °C, and the flow rate was varied from 7 sccm to 80 standard cubic centimeter per minute (sccm) resulting in doping levels ranging from $5 \cdot 10^{16}$ cm^{-3} to $1.2 \cdot 10^{18}$ cm^{-3}. No degradation in surface morphology and x-ray FWHM was observed.

P-type doping was achieved by Zn using DEZn as a source. For photodetectors operating at near room temperatures, low p-type doping is desirable. But because of high diffusivity of Zn, a lot of care should be taken to control the p-type doping level by Zn. A small mass flow controller with a 10 sccm capacity was used in order to better control the low flows. Prior to this work, we had reduced net acceptor concentration to $3 \cdot 10^{18}$ cm^{-3} using DMZn. This suggested that by using DEZn, whose vapor pressures is about 10 times lower than that of DMZn at a given temperature, the doping levels can be

brought down to 10^{17}cm^{-3} range. With the bubbler maintained at 10 °C, the flow of DEZn was varied from 0.05 sccm to 0.2 sccm. The resulting doping levels ranged from 2.5·10^{17}cm^{-3} to 7.5·10^{17}cm^{-3}.

3.2 InAsSb

3.2.1 Growth

The growth of InAsSb was attempted using 5 % arsine diluted in hydrogen as the As source. Later, for better control of arsine 0.2 % arsine has been used. The substrate preparation and pre-growth heating procedures for each substrates were identical to those for InSb growth. Starting with the best growth conditions for InSb, a small flow of diluted arsine was sent to the reactor to confirm the growth of InAsSb ternary. Once this was determined, the diluted arsine flow rate was varied to change the As composition. Increased arsine composition has been obtained by increasing arsine flow rate. The growth rate 0.7 μm/hr of InAsSb layer was found to be considerably lower than that of InSb (1.1 μm/hr) at the same growth condition. It indicates that some gas phase reactions may be taking place between the involved sources during InAsSb growth that lead to lower growth efficiency.

3.2.2 Characterization

The grown layers showed shiny surfaces under optical microscope indicating good morphologies. The alloy composition was estimated from X-ray diffraction data using Vegard's law. The x-ray diffraction peak of InAsSb was found to be broader than that of InSb of comparable thickness, despite the good morphologies of InAsSb films. The broadness is probably due to a large number of misfit dislocations and some compositional variations in the epitaxial layers.
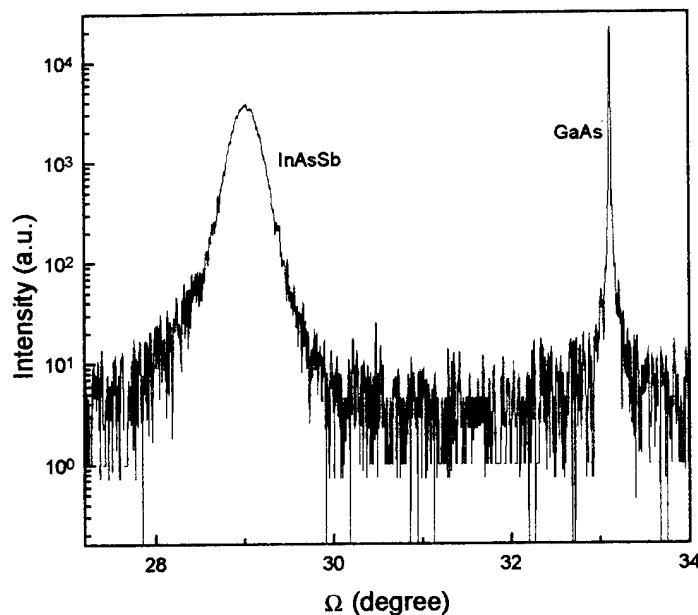

Fig. 8. X-ray diffraction spectra of 2 μm InAs$_{0.3}$Sb$_{0.7}$ layer grown on GaAs substrate.

Nominally undoped InAsSb layer showed negative Hall coefficient in the 4 to 300 K temperature range. The carrier concentration and Hall mobility at 77 K were 1-6·10^{16} cm^{-3} and 5,000-12,000 cm^2/Vs respectively for 2 μm thick samples. At 300 K, carrier concentration increased to 9-15·10^{16} cm^{-3} and Hall mobility increased to 13,000-25,000 cm^2/Vs. The strange behavior of these data suggested that the

14

InAsSb layer can be p-type. Theoretical calculation carried out at the CQD showed that with a shallow p-type background doping density of $5 \cdot 10^{15}$ cm^{-3} and dislocation density in the order of 2.5-$5 \cdot 10^{8}$ cm^{-2}, calculated data could agree with the experimental data for $InAs_{0.3}Sb_{0.7}$ layer.

Optical characterizations on these layers have been performed using Fourier transform infrared (FTIR) spectroscopy. Bandgap variation by changing the As composition can clearly be observed. Optical bandgap was determined as photon energy for which absorption coefficient is equal to 500 cm^{-1}. A bandgap of 103 meV was derived for $InAs_{1-x}Sb_x$ layer with x=0.77. An even narrower bandgap of 83 meV has been obtained for x=0.65. This shows that InAsSb can be used for the near room temperature photodetectors operating in the 8-14 µm spectral range.
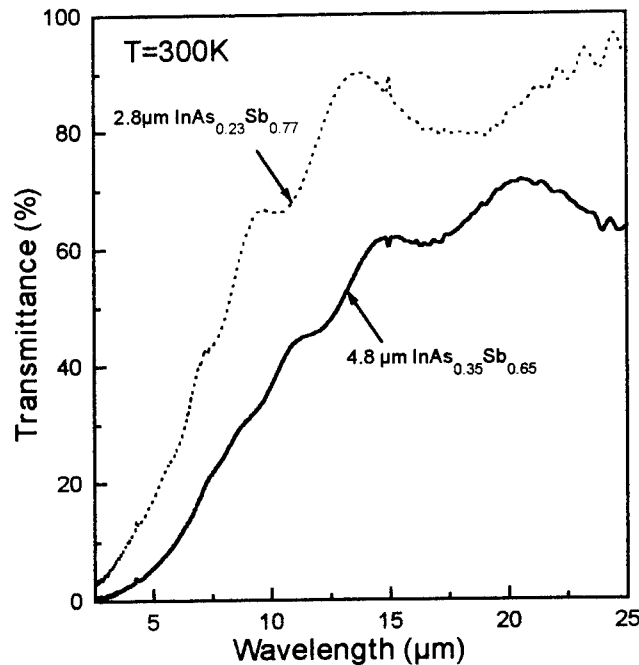

Fig. 9. Transmission spectra of InAsSb with different compositions.

3.2.3 Doping

N-type doping was obtained by using TESn as the Sn dopant source. The doping characteristics of the InAsSb layer was similar to that of InSb. As low p-type doping (order of 10^{16} cm^{-3}) is ideal for near room temperature photodetectors, much effort has been devoted to decrease the p-type doping level. DEZn with bubbler temperature of 10 °C has resulted in doping levels of 3-$5 \cdot 10^{17}$ cm^{-3} with flow rate of 0.015-0.02 sccm. For realization of $\sim 10^{16}$ cm^{-3}, the temperature of DEZn bubbler has been lowered to around -15°C where the vapor pressure is approximately 5 times lower than at 10°C. By controlling the mass flow to 0.01 sccm, we could obtain the doping level of $3 \cdot 10^{16}$ cm^{-3}.

3.3 GaSb

Recently, GaSb has been grown on both GaSb and GaAs substrate. GaSb can be used as a buffer layer for the growth of InSb and InAsSb on GaAs. Another possibility is that a GaInSb lattice matched to InAsSb can be useful as a barrier in InAsSb photodetectors. For the later growth of GaInSb layer, growth technology of GaSb needs to be developed.

Triethylgallium (TEGa) and trimethylantimony (TMSb) have been used for GaSb growth. Both bubblers were kept at temperature of 0°C resulting in vapor pressure of 1.21 and 30.95 torr, respectively. The GaSb substrate has been degreased by trichloroethylene, acetone and alcohol. Then, it

15

was etched by bromine/methanol solution just before the growth and immediately transferred to the reactor to prevent any oxidation. The growth temperature was kept at 500°C, and the optimized V/III ratio was around 8. Dependence of surface morphology and crystallinity on the V/III ratio was similar to that of InSb growth. A preliminary grown 1.2 μm thick sample showed x-ray FWHM of 88.2 arsec on GaSb substrate and 348 arsec on GaAs substrate. In both cases, the morphology observed by optical microscope was good with some dislocations. These preliminary growths have already shown the promise for high quality GaSb and GaInSb layers.

3.4 Detector Structures
3.4.1 InSb p-n structure

Undoped InSb was verified to be n-type from the low temperature Hall measurement. Thus, the growth of InSb p-n diode for photodetector application has been attempted using only the p-type dopant source. The growth has been carried out on semi-insulating GaAs substrate. After growing undoped (n-type) InSb layer for 2.5 μm, 0.2 μm of p-type InSb layer has been grown. As relatively high p-type doping level is desirable for top p-type layer, we used DMZn as a Zn dopant source.

3.4.2 InAsSb photoconductor structure

At near room temperatures, low p-type ($10^{16}\,cm^{-3}$) is expected to be the optimum doping level for long-wavelength photodetector applications. P-InAsSb/p-InSb has been chosen for photoconductivity studies. InSb was expected to act as both the buffer layer for growth and the carrier confinement layer. Because low doping was required for the layers, DEZn kept at -15°C was used as a dopant source. The mass flow of hydrogen to DEZn bubbler was 0.01 sccm. The standard structure consisted of 1 μm InSb buffer layer and 3 μm InAsSb active layer.

As grown samples had mirror-like surface morphology. Structural characterization was performed using x-ray diffraction at (400) orientation. As shown in the figure, clearly defined peaks for InSb and InAsSb were resolved with low FWHM values. Composition of the InAsSb layers have been determined by Vegard's law.
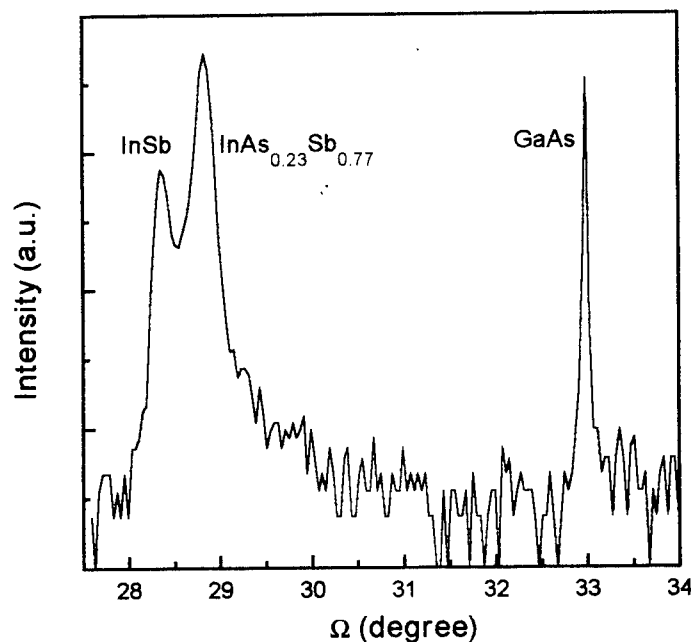

Fig. 10. X-ray diffraction spectra of InAsSb photodetector structure.

Hall measurements exhibited n-type conductivity at 300 K with the electron concentration of $3 \cdot 10^{16} \text{cm}^{-3}$ and a mobility of 36,000 cm^2/Vs. At 77 K, p-type conductivity was observed with the hole concentration of $3.6 \cdot 10^{16} \text{cm}^{-3}$ and a mobility of 923 cm^2/Vs. This behavior of Hall data was expected for p-type materials. Knowing that the InAsSb layer dominates the Hall coefficient at room temperature, our obtained value of electron mobility was higher than the MBE value with comparable thickness.

3.4.3 InAsSb photovoltaic detector structure

To realize photovoltaic detectors, we have grown several photodiode structures with an InAsSb active layer. It consisted of n$^+$-InSb contact layer, π-InAsSb active layer and p$^+$-InSb contact layer. Doping levels of each layer were $1 \cdot 10^{18} \text{cm}^{-3}$, $3\text{-}20 \cdot 10^{16}$ cm^{-3} and $1 \cdot 10^{17} \text{cm}^{-3}$ respectively. InSb layer was chosen as contact layers for both p- and n-type because we could use well developed InSb technology. From the band diagram study, this structure was expected to give high gain in the entire InAsSb active layer. To obtain higher detectivity, a relatively thick InAsSb active layer (about 5 μm) was needed to increase the quantum efficiency. Including the 2μm thick n$^+$-InSb layer and 0.5 μm thick p$^+$-InSb, the total layer thickness was around 7.5 μm. This increased total growth time to 11 hours. As the reactor tube is contaminated during the long growth, it was relatively difficult to get entire layers with good morphology. To prevent this problem, regrowth technique of the layers is currently under investigation.

Grown layers have been characterized by different techniques. Surface roughness has been measured by alpha step, and the thickness was measured by ball polishing measurement. As accurate control of etching is required for detector fabrication, the thickness of the layer needed to be measured precisely. X-ray measurement showed clearly resolved peaks for different layers.

4. Device processing

The most important points in fabricating photodetectors are to get a mesa structure, the contact, and its pattern. The process steps are mainly cleaning of wafer, photolithography pattern for the mesa structure and the contacts, etching of the mesa structure, metallization, etching of the contact pattern, and wire-bonding and package.

4.1 Photoconductive detectors

The processing of a photoconductive detector is quite simple. The cross-section of a photoconductive detector is schematically shown in Fig. 11. The cleaning process is the same as that of photovoltaic detector process, which is described in the following section. 500 Å-Ti and 3000 Å-Au are evaporated by an electron-beam-evaporator. The contact pattern is made by using a metal-mask, which covers some parts of the surface during the evaporation. The active area is 3×4 mm^2.

Ti/Au   Ti/Au

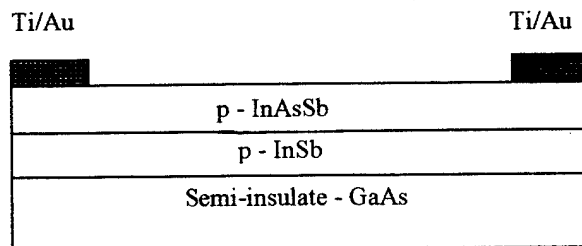| p - InAsSb |
| --- |
| p - InSb |
| Semi-insulate - GaAs |

Fig. 11. The cross section of InAsSb photoconductive detector.

17

4.2 Photovoltaic detectors

The cross-section of the photovoltaic detectors is schematically shown in Fig. 12. The contacts are on the p and n-type region. The sensitive area is $400 \times 400 \ \mu m^2$. The top contact is on the sensitive area which is $150 \times 150 \ \mu m^2$. The bottom contact is made on the bottom layer, which is $100 \times 250 \ \mu m^2$. Such a structure is suitable for the operation of back-side illumination. The Au-wire is directly bonded on p-type region which could damage the material.
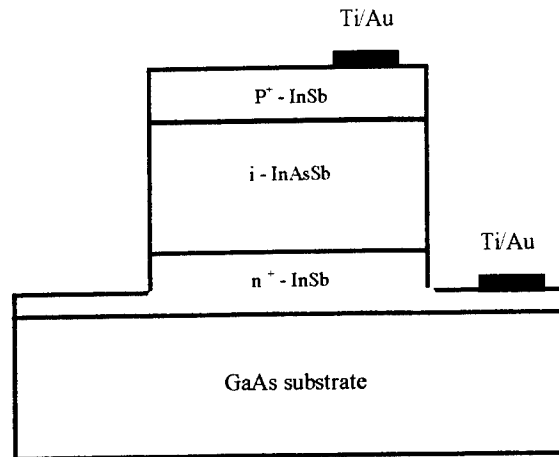
Ti/Au

P⁺ - InSb

i - InAsSb

Ti/Au

n⁺ - InSb

GaAs substrate

Fig. 12. The cross section of InAsSb photodetector with p-i-n structure.

Before the wafer is processed, the cleaning process is done by using boiling solvents: TCE, TCA, acetone, methanol, and propanol. The next step is to etch the mesa structure. This is accomplished by using photolithography and chemical etching techniques.

Photolithography technique is used to make the pattern of mesa structure for chemical etching. The photoresist (Shipley 1813) is deposited at a rotation of 5000 rpm. The corresponding thickness is about 1 μm which is measured by an alpha-step (Tencor).

The photoresist is pre-baked inside the oven at temperature 80°C for 30 minutes. The wafer is aligned with the Cr-mask with the mesa pattern in the UV aligner machine (Karl-Suss). The exposure time is about 12 seconds. The mesa pattern with photoresist is developed by using the mixed solution (Shipley Developer 351: H_2O = 1:5) for 1 minute. The wafer is then post-baked for another 30 minutes at temperature 120 °C.

The mesa pattern is made by wet chemical etching at room temperature. The mixed chemical solution is lactic and nitric acids (10:1). The etching rate is about 2 μm/min. However, it is dependent on the quality of epitaxial layers. The detailed process steps are schematically illustrated in Fig. 13 (a) - (d).

The next important step is to make the metallization and contact pattern. Ti and Au are used to make contacts for InAsSb devices. Ti exhibits good adhesion with semiconductor surface and has good stability. As one of its disadvantages, the melting temperature of Ti is about 1800 °C, which makes it difficult to evaporate in a normal thermal evaporator. Au and its alloys are commonly used to make contacts in combination with Ti in narrow-gap semiconductors. It is easy to make Au-wire to bond with Au contact. 500 Å Ti and 3000 Å Au are evaporated by an electron-beam-evaporator (CHA Industries, SR-10).
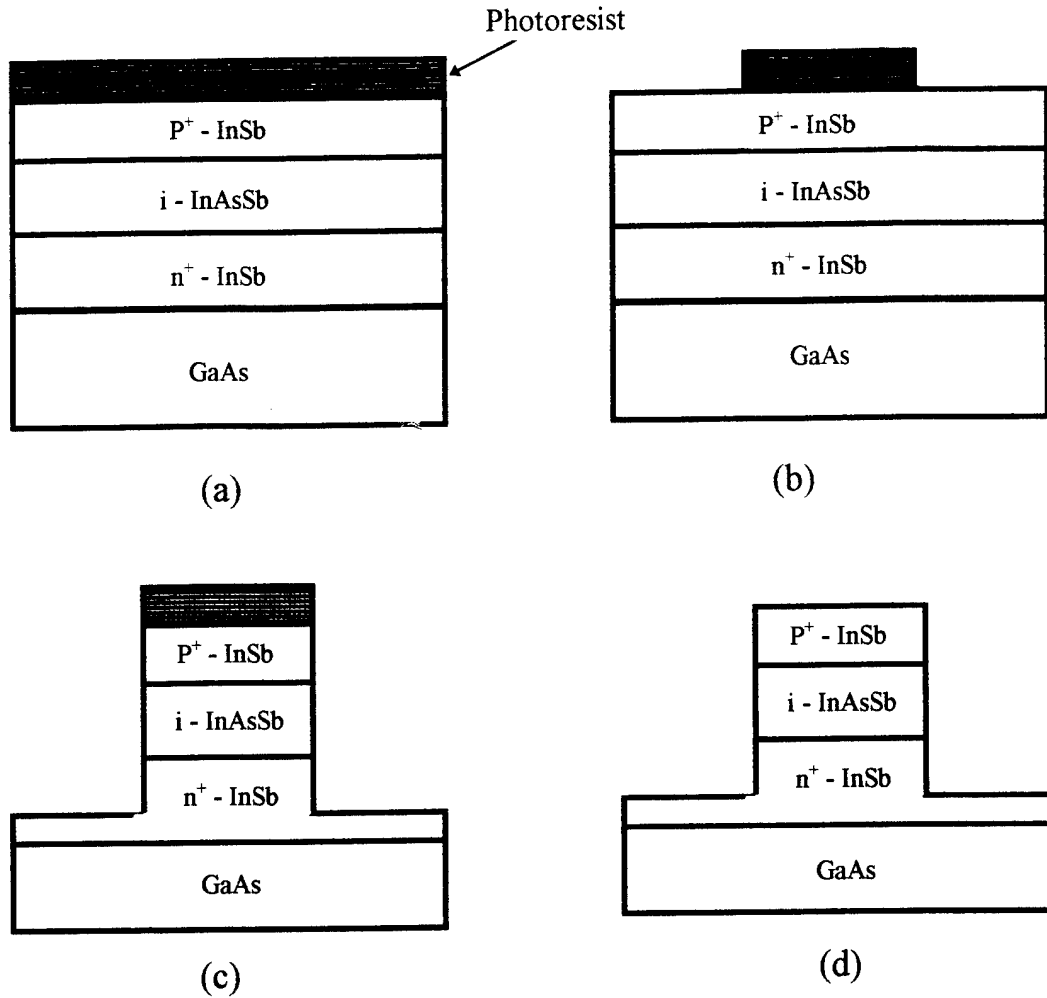
Fig. 13. The process steps for etching the mesa structure.

The contact pattern is made by using the photolithography technique and wet chemical etching. The etching solution for Au is $KI_2 : I_2 : H_2O$ (40 g : 3 g : 100 ml). I_2 could damage the surface of InSb. The Au-etching solution ($KI_2 : I_2 : H_2O$) is highly selective which cannot etch Ti. The Au etching time is 15 seconds. The Ti-etching solution ($HF : H_2O = 5 : 100$) is also selective, which cannot etch InAsSb and other III-V materials. The Ti-etching time is 10 seconds. The detailed process steps are schematically illustrated in Figure 14 (a)-(d).

The photodetector chips are mounted on the heat-sink made from copper by using 2-ton epoxy. The Au-ball bonding is made in a Universal Ball Bonder (Kullicke and Soffa Industries Inc., Model 4124). Since InSb is mechanically quite soft material, special care has to be taken by adjusting the force, power, time and temperature for bonding when the bonding point is made on the sensitive area. A temperature around 137 °C and a time of about 500 ms are used.
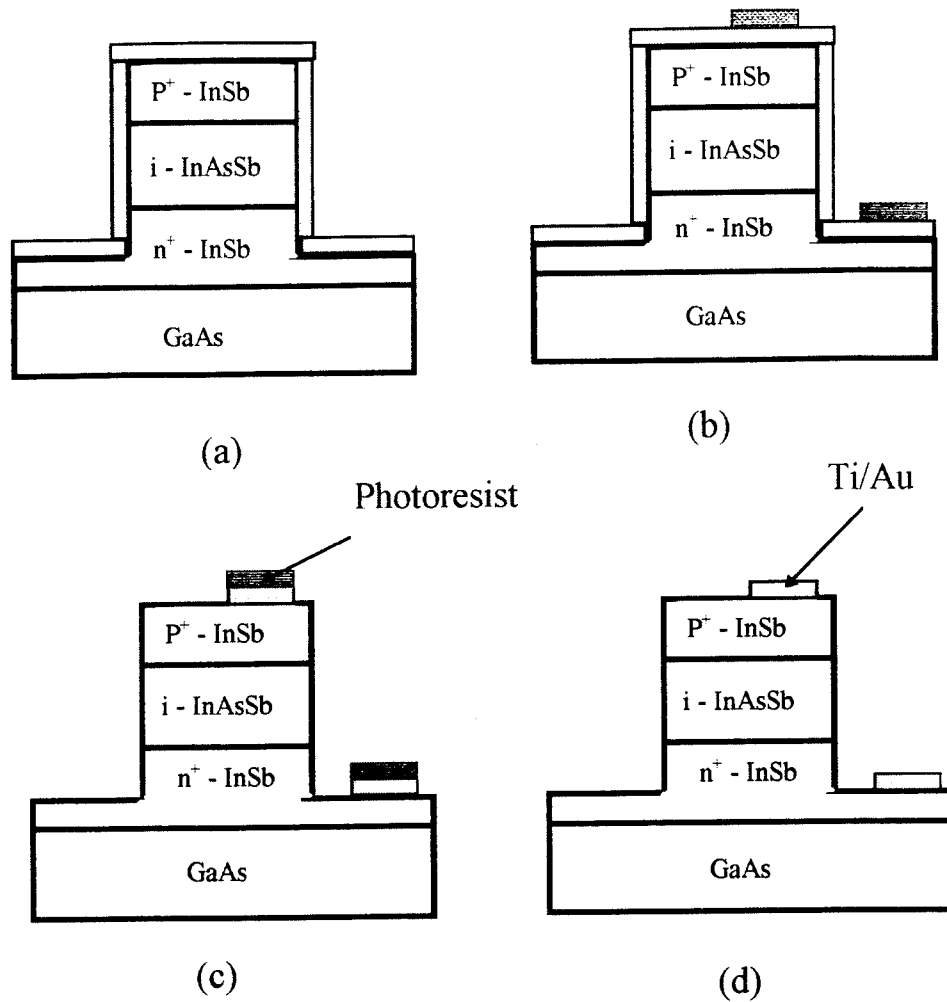
(a)

(b)

Photoresist

Ti/Au

(c)

(d)

Fig. 14. The process steps for etching of the contact pattern.

5. Experimental photodetectors

5.1. Photoconductors

p-InAsSb/p-InSb/GaAs heterostructure has been chosen for photoconductivity studies for a number of reasons. InAsSb has been selected as the absorber material of heterojunction photodetector, its p-doping level has been selected for the best performance at 200-300 K. InSb was used as a buffer layer with lattice constant close ($\approx$2% mismatch) to that of InAsSb with compositions optimized for operation in the 8-14 μm. Another supposed role of InSb was electron confinement for electrons in the absorber layer to prevent recombination of minority carriers at absorber-substrate interface. P-type doping of InSb layer should reduce its shunting effect. GaAs is a common, high-quality, and low-cost substrate which is perfectly transparent in a wide spectral range. This makes it possible to use backside illumination both for the research purposes and to improve performance in practical applications. GaAs is expected to be used in future for monolithic optical immersion of the detectors to lenses formed directly in the substrate material.

Triple layer p-InSb/p-InAsSb/p-InSb/GaAs heterostructures have also been used in order to establish the influence of the p-InSb coating on the surface properties. The additional p-InSb layer has been used to check how the device properties are limited by recombination at the top surface.
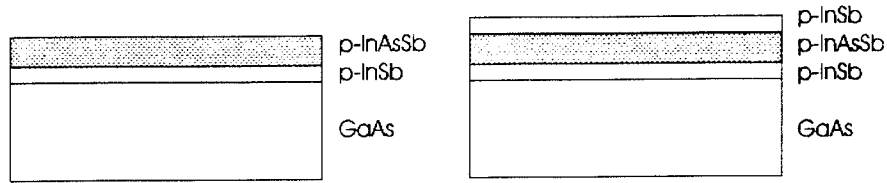
20

p-InAsSb
p-InSb

GaAs

p-InSb
p-InAsSb
p-InSb

GaAs

Fig. 15. Geometry of double and triple layer heterostructure photoconductors.

InSb   InAsSb

E_c

E_F
E_v

InSb   InAsSb

E_c
E_F

E_v

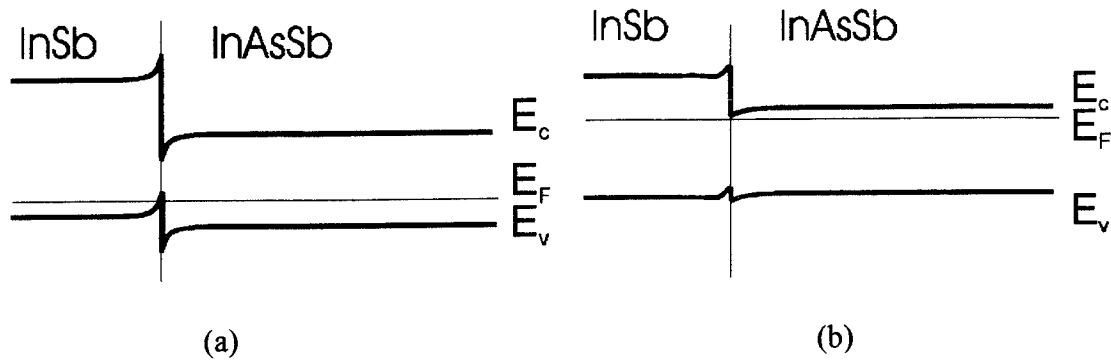(a)   (b)

Fig. 16. Schematic band structure of ideal p-InSb/pInAsSb heterojunctions:
(a)- at low temperatures, (b)- at near room temperature.

Fig. 15. shows the geometry of the device. Schematic band diagrams of double layer heterostructures at low and high temperature are illustrated in Fig. 16.

Photoconductivity has been measured using double and triple layer heterostructures with the same nominal doping of all layers. Fig. 17 shows the spectral responsivities of the photoconductor sample at various temperatures.
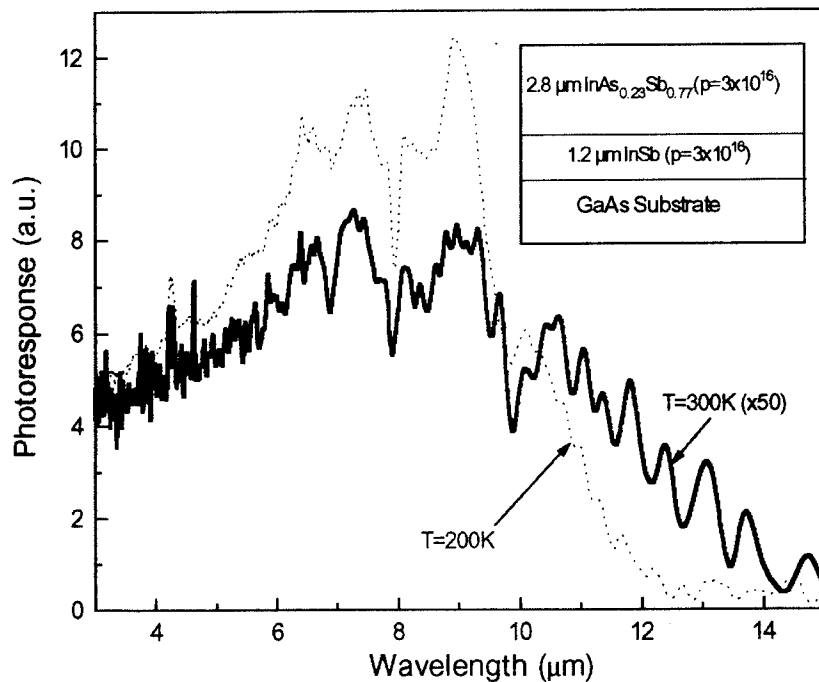

Fig. 17 . Spectral photoresponse of the photoconductive structure.

The spectral response could be measured at room temperature up to wavelengths exceeding 13 μm despite the doping of the layer not being optimized for room temperature operation. To our best knowledge, these measurements were the first observation of true room temperature photoresponse (not thermal response) at such a long wavelength. The evidences that the photoresponse is due to photoconductivity rather than thermal response are a normal dependence of spectral curves on temperature, low response at wavelength beyond fundamental absorption, and good agreement with absorption curves.

Measurements of frequency response of the photoconductors exhibit a weak thermal effect response at low frequencies. At low frequencies, the measured signal decreases with frequency; achieving frequency independent level at relatively low frequencies (<200 Hz), however. This is evidence of some contribution of bolometric effect at low frequencies. The contribution of thermal response was negligible at frequencies used by FTIR measurements (f>1200 Hz). The relatively low thermal response compared to that of MCT/CdTe is mostly due to much higher thermal conductivity of GaAs (0.5 W/cmK) compared to that of CdTe (≈0.05W/cmK).

Low temperature (T ≤ 150 K) measurements exhibited some contribution of photovoltaic response especially for backside illumination. To prevent this, contact regions were masked from incident radiation with metal foil.

Absolute measurements of photoconductivity response were used for determination of $\mu_e\tau$ product and effective lifetime. Table 1 shows results of photoconductivity measurements with frontside illumination, which can be used for lifetime determination.

As Table 1 shows, the peak voltage responsivity measured in constant current bias increases with reduced temperature. This can be mainly due to the increased sample resistance. The measured $\mu_e\tau$ product decreases as temperature decreases and achieves its minimum at 150 K and increases with further cooling.

The electron mobility is known only at room temperature where intrinsic electrons dominate Hall effect. The stationary photoconductivity effective lifetime at room temperature (≈ 0.7 ns) is relatively long for E_g≈0.1 eV material at 300 K. Even longer effective lifetime can be obtained for optimized p-doping. This value of lifetime makes it possible to obtain relatively good responsivity. For devices on 0.2 mm thick GaAs substrate fixed to metal base for good heat dissipation, the thermal resistance is about 4 K/W for 1×1 mm² device. Therefore, power dissipation density of 1 W/mm² can be applied with temperature increase by 4 K. This corresponds to an electrical field exceeding 40 V/mm.

Table 1. Results of photoconductivity measurements.

T (K)	V_b (V)	R (Ω)	V(μV)	R_v^{BB} (V/W)	R_{vp} (V/W)	$\mu_e\tau$ (cm²/Vs)	τ (ns)
77	3.4	469	35.2	$2.24\cdot10^{-1}$	$4.65\cdot10^{-1}$	$1.48\cdot10^{-5}$	
150	3.6	557	12.4	$7.88\cdot10^{-2}$	$1.28\cdot10^{-1}$	$3.62\cdot10^{-6}$	
200	2.6	334	18.0	$1.14\cdot10^{-1}$	$1.81\cdot10^{-1}$	$8.22\cdot10^{-6}$	
250	0.78	54.3	2.05	$1.3\cdot10^{-2}$	$1.95\cdot10^{-2}$	$2.33\cdot10^{-5}$	
300	0.28	18	0.18	$1.14\cdot10^{-3}$	$2.10\cdot10^{-3}$	$2.46\cdot10^{-5}$	0.7

The photoconductive lifetime at 300 K (0.7 ns) is close to the theoretical limit set by Auger recombination in 0.103 eV material. The agreement is quite good taking into account factors of a great uncertainty involved in the theoretical calculations.

The voltage responsivity of ≈ 0.25 V/W at 10.6 μm can be obtained for 1 mm wide detectors assuming 1W/mm² bias power dissipation according to eqn. (7). Therefore, the Johnson noise limit of

detectivity of the photoconductor at room temperature is $\approx 4\cdot10^{7}\,\mathrm{cmHz^{1/2}/W}$. This is below the theoretical limit set by the generation-recombination processes in the material ($\approx 1.5\cdot10^{8}\,\mathrm{cmHz^{1\,2}/W}$).

A much thinner substrate would be necessary to achieve bias dissipation required for generation-recombination noise to dominate. The heat dissipation constraints are much relaxed in small size devices, with length and width smaller than the substrate thickness due to three-dimensional heat dissipation. This would make it possible to achieve the generation-recombination limit in small size devices.

An example is optically immersed devices, where actual detector size is highly reduced compared to the apparent optical size. GaAs substrate (n=3.3) can be used as a material for formation of immersion lens. Despite the usual gain due to optical immersion (n or n^2), additional gain is expected from increased relative heat dissipation capability. Optically immersed photoconductors can achieve detectivity of $\approx 10^{9}\,\mathrm{cmHz^{1/2}/W}$ at 300 K.

In contrast to theoretical prediction, the $\mu_e\tau$ product and τ itself at lower temperatures are quite low. The low temperature electron mobility is not known, therefore, we cannot determine the recombination time from stationary photoconductivity and low temperature. The possible reasons for a short lifetime are non-fundamental recombination mechanisms, such as Shockly-Read-Hall, surface or interface recombination. The time necessary for electron to diffuse through the layer thickness is

$$\tau_D = \frac{t^2}{2D_e} \tag{22}$$

where D_e is the electron diffusion coefficient. According to Einstein relation $D_e = kT\mu_e/q$ and

$$\tau_D\mu_e = \frac{t^2 q}{2kT} \tag{23}$$

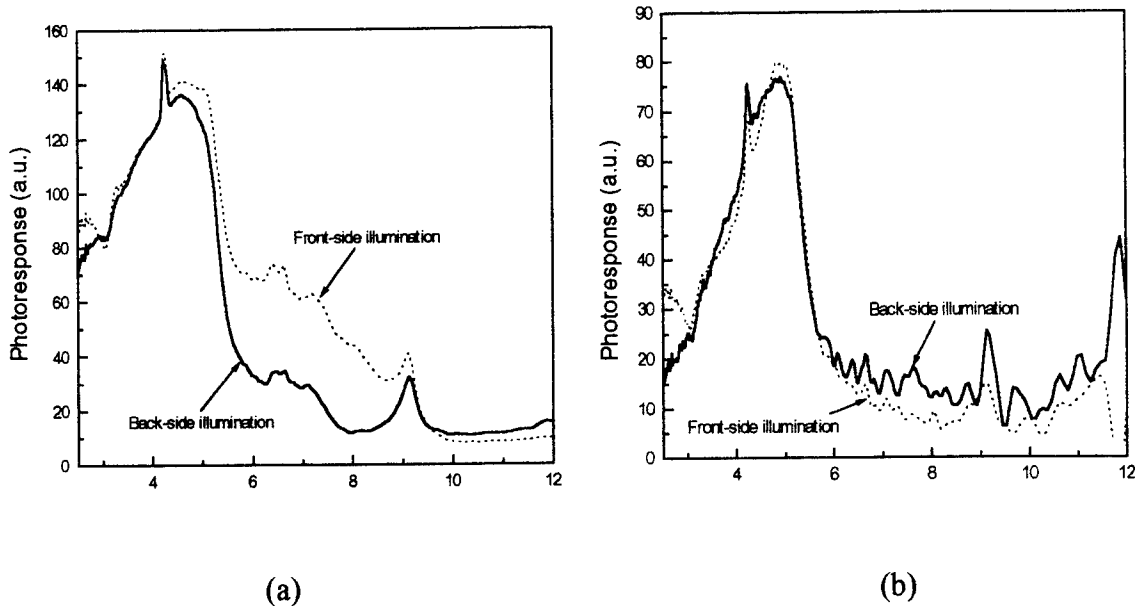(a)   (b)

Fig. 18. Spectral photoresponse of the double (a) and triple (b) layer heterostructures at 77 K.

At a temperature of 150 K, the calculated $\mu_e\tau_D$ value is $\approx 1.5\cdot10^{-6}\,\mathrm{cm^2/Vs}$ (t=2.8 μm). Taking into account that the generation of carriers occurs not only at the surface but within entire layer thickness

and that the interface recombination velocity has a finite value, the calculated diffusion limited lifetime-electron mobility product is comparable to the experimental values.

Low temperature spectra of InAsSb/InSb/GaAs heterostructures, in contrast to those at near room temperatures, exhibit significant differences if illuminated from front- and backside. At first, relatively high photoresponse is observed in the short-wavelength region with the cutoff at ≈ 5.5 μm. InSb layer, with higher time constant, seems to be responsible for the short-wavelength response. The long-wavelength response due to the InAsSb layer is strongly dependent on illumination direction; frontside illumination yields a better response (Fig. 16a). This seems to be direct evidence of deleterious effect of InSb/InAsSb interface on photoconductivity. Covering the InAsSb with additional InSb layer reduced the frontside illumination (Fig. 16b).

Therefore, we can expect that the effective lifetime at low temperatures may be controlled by recombination at the InSb/InAsSb interface. Lattice matched buffer layer, such as InGaSb seems to be necessary to improve the performance of the photodetectors at temperatures below 300 K.

Conclusions:
1. The high value of lifetime combined with a good thermal conductivity of GaAs substrate makes it possible to achieve good performance of the photoconductive detector at room temperature with a detectivity of about $4 \cdot 10^7$ cmHz$^{1/2}$/W. This exceeds the performance of HgCdTe photodetectors operated at the same conditions.
2. The performance of the devices can be significantly improved to the level of $\approx 10^9$ cmHz$^{1/2}$/W by the use of monolithic optical immersion with lenses directly prepared in GaAs substrates. This makes the device attractive for some applications as 10.6 μm laser radiation detection and monitoring, and heterodyne detection when bandwidths of several hundreds MHz are required.
3. In contrast, the PC devices exhibit quite poor performance at low temperatures. It is expected that the low temperature photoconductivity is limited by interface recombination. The photoconductive lifetime in this case may be determined by the time required for carriers to diffuse to the interface region. This seems to be due to poor InSb/InAsSb interface properties.
4. The use of a buffer lattice matched layer seems to be necessary for better performance at low temperatures. InGaSb, with low Ga fraction, lattice matched to InAsSb layer seems to be a good candidate for the buffer layer.

5.2 Photovoltaic detectors

Current-voltage curves have been measured using the Hewlett-Packard semiconductor analyzer. The relative photovoltaic spectra were measured with FTIR spectrophotometer comparing the measured and internal pyroelectric detector responses, and by correcting for the slow frequency of the pyroelectric detector. The absolute responsivity was determined using 800 K blackbody response measurements.

The photovoltaic spectral response could be measured at room temperature up to wavelengths exceeding 13 μm. To our best knowledge, these measurements were the first observation of true room temperature photovoltaic response at such a long wavelength. The evidence that the photoresponse is due to photovoltaic effect rather than thermal response are normal dependence of spectral curves on temperature, very low response at wavelength beyond fundamental absorption, and good agreement with the absorption curves.
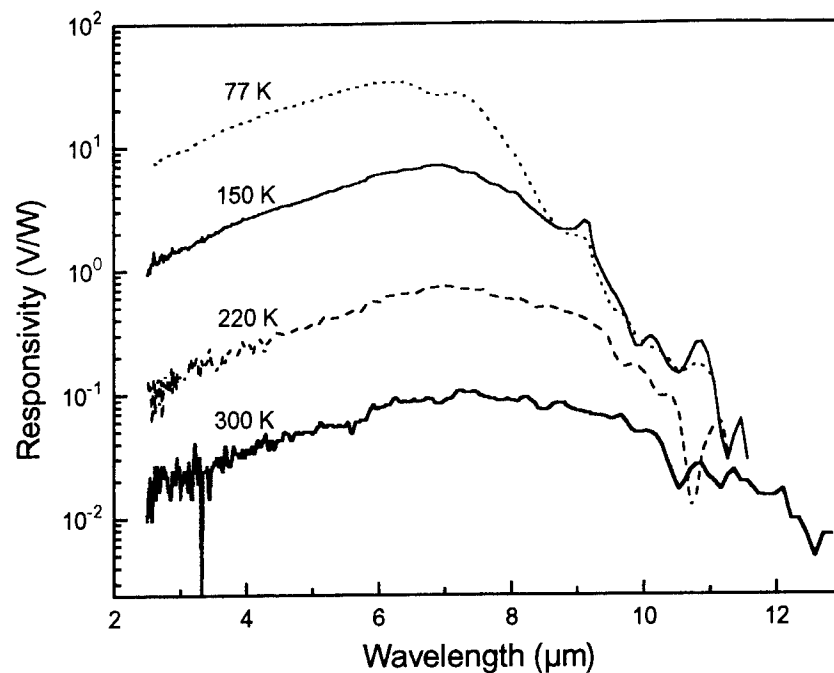
Fig. 19. Spectral response of photovoltaic detector as a function of temperature.

Measurements of frequency response of the photovoltaic detectors exhibit weak thermal effect response at low frequencies. At low frequencies, the measured signal decreases with frequency: achieving frequency independent level at relatively low frequencies ($\approx$200 Hz), however. This is evidence of some contribution of the Seebeck effect at low frequencies. The contribution of thermal response was negligible at frequencies used by FTIR measurements (f>1200 Hz). The relatively low thermal response compared to that of MCT/CdTe is mostly due to high thermal conductivity of GaAs.

Absolute measurements of photovoltaic response were used for determination of the voltage responsivity-area product. Table 2 shows the measured resistance, 800 K blackbody voltage responsivity, peak responsivity, and voltage-area product as a function of temperature.

Tab. 2. Properties of longwavelength n^+-InSb/p-InAsSb/p^+-InSb photovoltaic detectors as a function of temperature. Doping of InAsSb was $2 \cdot 10^{17}$ cm^{-3}.

T, K	R, Ω	R_{vb}, V/W	R_v, V/W	R_vA, V·cm^2/W
77	194	12.25	28.5	4.56×10^{-2}
100	181.9	6.77	16.1	2.58×10^{-2}
150	168.8	2.53	6.05	9.68×10^{-3}
200	158.3	0.41	1.027	1.64×10^{-3}
220	155.7	0.248	0.642	1.03×10^{-3}
250	151.9	0.138	0.348	5.57×10^{-4}
300	142.2	0.0358	0.0913	1.46×10^{-4}

As Tab. 2 shows, the voltage responsivity increases with increasing temperature, but the increase is much less steep compared to the calculations based on the simple generation-recombination model. While the responsivity at room temperature is within a factor 3 below the theoretical predictions and

25

close to that for HgCdTe photodiodes operated at the same conditions, the performance at low temperatures is by many orders of magnitude lower than expected from the fundamental thermal generation. The possible reasons are high level doping resulting in high tunnel dark current and the poor interface properties due to lattice mismatch between the absorber and contact regions.

Series resistance of the photovoltaic detectors was initially higher than $100\ \Omega$. Improvement of metallization has resulted in reduction of the series resistances to below 10 ohms. Measurements of the resistances between adjacent contacts to n^+ layers yielded lower resistances. The estimated resistances of the neutral region of the devices and the room temperature junction itself was well below $1\ \Omega$. Therefore, we believe that the series resistance of the devices was mainly due to contact resistance to p^+-layer. The high series resistances dominates the total resistance of the device at near room temperatures and reduces the detectivity. An exception is very small size devices (few μm^2) when junction resistance may dominate.

Conclusions:

The device described in this report is our first attempt to produce an InAsSb long-wavelength photovoltaic detector operating at near room temperature. The devices exhibit measured sensitivity up to $\approx 14\ \mu m$ at room temperature. The voltage response-area product at room temperature is close to that for HgCdTe devices operating at $10.6\ \mu m$. In practice, the normalized detectivity was limited by the Johnson noise of the series resistance. This noise will dominate the noise of room temperature photodetectors with the exception of very small area devices. The performance can be much improved by the use of optical immersion which improves the ratio of the junction to the series resistances and increases the voltage responsivity in comparison with the non-immersed device of the same optical area.

The low temperature performance was poor. To improve, it would be necessary to optimize doping and to use lattice matched heterojunction device.

In summary, this preliminary work has demonstrated room temperature InAsSb photodetectors operating up to $\approx 14\ \mu m$ with performance close to the theoretical limits determined by fundamental limitations. The present InAsSb devices may be already useful for some applications (CO_2 laser monitors, laser warning receivers and others). The monolithic optical immersion should increase the performance to the level comparable to the state-of-art microbolometers, but with much faster speed of response. Further optimization of devices and the use of simple Peltier coolers should bring even improved performance, so that this technology may become a serious challenger to both MCT and microbolometer technologies.

6. Future works

The development of InAsSb infrared photodetectors is by no means finished yet. The main efforts to be done should be:

- Reproducible growth of heterostructure with required band gap and doping profiles.
- Growth of contact regions with wider gap and lattice matched to the absorber region. This is equally important to both photoconductors and photovoltaic detectors.
- Passivation of the side surfaces to prevent additional contributions to the dark current of the devices.
- Reduction of series resistances due to the contact resistances of $p^+\pi$, $n^+\pi$ and distributed resistances along bottom n^+-layer. The contact resistances of $p^+\pi$ seems to be dominant.
- Investigation of interface and surface properties of the heterostructures.
- Improvement of device processing technology; this relates particularly to p^+-region contacts. The full area of the photodiode should be metallized for better quantum efficiency.

- The use of a self-consistent iterative procedure for the solution of Van Roosbroeck mathematical model for InAsSb-based heterojunction devices including multijunction devices.
- Development of the stack multijunction technology.
- Development of monolithic optical concentrators.
- Development of the hybridization of the individual elements to a silicon signal processing chip.
- Development of InAsSb-based long-wavelength IR focal plane arrays.

7. Related papers

- Piotrowski and M. M. Razeghi, "Improved performance of IR photodetectors with 3D gap engineering", Proc. SPIE (to be published, 1995).
- J. Piotrowski and M. Razeghi, "Near room temperature longwavelength photodetectors", proposal delivered to NSF (1995).
- D. Kim, D. Wu, J. Wojkowski, J. Piotrowski, J. Xu, and M. Razeghi, "Long-wavelength (8-14 μm) InAsSb photoconductors operated at near room temperatures (200-300 K)", submitted for publication in APL (1995).
- D. Kim, D. Wu, J. Wojkowski, J. Piotrowski, J. Xu, and M. Razeghi, "MOCVD grown heterojunction 8-12 μm InAsSb photodiode operating at near room temperatures", submitted for publication in APL (1995).